

# We are IntechOpen, the world's leading publisher of Open Access books Built by scientists, for scientists

6,900

Open access books available

186,000

International authors and editors

200M

Downloads

Our authors are among the

154

Countries delivered to

TOP 1%

most cited scientists

12.2%

Contributors from top 500 universities



WEB OF SCIENCE™

Selection of our books indexed in the Book Citation Index  
in Web of Science™ Core Collection (BKCI)

Interested in publishing with us?  
Contact [book.department@intechopen.com](mailto:book.department@intechopen.com)

Numbers displayed above are based on latest data collected.  
For more information visit [www.intechopen.com](http://www.intechopen.com)



# Technologies of High-Temperature Insulating Coatings on Stainless Steels

*Zoia Duriagina, Taras Kovbasyuk, Volodymyr Kulyk, Andriy Trostianchyn and Tetiana Tepla*

## Abstract

For the use of chromium steels in instrumentation, microelectronics, and electrical engineering, their surfaces are additionally protected by coatings based on glass ceramics and other insulating materials. Such materials can operate at high temperatures for a long time under the influence of the electric current or magnetic field. This chapter describes the research results on synthesized coatings based on oxide glass ceramics and oxide materials obtained by plasma chemical vapor deposition (CVD) on the surfaces of stainless steels.

**Keywords:** insulating coatings, glass-ceramic coatings, oxide materials, stainless steel substrate

## 1. Introduction

It is known that the corrosion-mechanical and functional properties of steels can be improved by alloying elements with a more negative electrode potential (chromium, silicon, aluminum) or elements with a higher potential than iron (e.g., copper, molybdenum, nickel) or elements that promote the formation of carbides, nitrides, and other phases.

The second way (which can occur simultaneously with the first) is to use various methods of surface engineering, in particular, the formation of a dense oxide film, which protects the surface of the alloy from oxidation and dissolution or acts as a functional coating, e.g., a dielectric one. To do this, you need to have the appropriate concentration of the alloying element. To ensure the proper level of functional properties, such coatings must be without defects, with high adhesion to the surface and minimal difference in thermal expansion coefficients as compared to the stainless steel substrate. The condition of formation of such coatings is a certain ratio of the volumes of oxide ( $V_{MeO}$ ) and the oxidizing metal ( $V_{Me}$ ):  $V_{MeO}/V_{Me} > 1$ . Under such a condition, as a rule, coatings are formed that improve the functional properties of the metal and slow down both the degradation process of its microstructure and deterioration of the properties.

As is known, stainless steels are obtained by introducing into the composition of low- and medium-carbon steels at least 12.5% chromium as well as nickel and other alloying elements (titanium, aluminum, molybdenum, niobium, copper, manganese). Depending on the structure, austenitic (AISI 302, 347, 316L, 316, 316Ti, and

others), ferritic (AISI 430, 430Ti, 439, and others), martensitic (AISI 420, 431, 420F), austenitic-martensitic (AISI 631, AM350), and austenitic-ferritic (AISI 301) stainless steels are distinguished. Chromium ferritic and chromium-nickel austenitic steels are the most common in engineering practice [1].

Chromium ferritic stainless steels are the cheapest, but they are inferior to chromium-nickel steels in corrosion resistance. So, AISI 430 steel is stable in acidic environments, but not suitable for welding, because during welding when heated above 900–950°C and rapidly cooled, the grain boundaries become depleted in chromium. With content less than 12% Cr, the electrochemical potential of the steel becomes negative, and it loses its ability to resist corrosion. Under these conditions, AISI 430 steel has a dangerous type of corrosion—intercrystalline corrosion. Stabilization of this steel with titanium or niobium is used to prevent this. It should be noted that  $\sigma$  phase (Fe, Cr) can be formed in high-chromium steels as a result of delamination of the alloyed solid solution into a mixture of  $\alpha + \alpha'$  phases (where  $\alpha'$  is  $\sigma$  phase). Due to this, the corrosion resistance of such steels is reduced. In ferritic steels with 20% Cr, the minimum formation time of the  $\sigma$  phase at 600°C is 150 h, and in the steels with 25% Cr at 650°C, it is 15 h. Therefore, when using these steels, it is desirable to bypass this temperature range.

## 2. Features of synthesis of glass-ceramic coatings on stainless steels

Ferritic and ferritic-martensitic stainless steels are widely used in electrical engineering as heat carriers and metal substrates for the manufacturing of film heating elements (FHE) (**Figure 1**). To insulate the metal substrate from the action of electric current, a dielectric insulation coating is applied to its surface. There are a large number of materials that can be used as electrical insulators at high temperatures. But for the correct choice of technology of a quality coating on the surface of stainless steel, it is necessary to take into account the coefficient of linear thermal expansion (CLTE) and the absence of phase transformations in the structure of the coating material during operation [2].

Due to the compatibility of thermal, physical, and micromechanical properties of stainless steels to the protective coatings, a material based on the fusible glass ceramics of the ZnO-PbO-B<sub>2</sub>O<sub>3</sub> system was proposed as a coating material [3–15].

For the preparation of coatings based on the PbO-ZnO-B<sub>2</sub>O<sub>3</sub> glass-crystal system, mixtures of powders, the compositions of which are shown in **Table 1**, were used. Each mixture was poured into an electrocorundum crucible and melted

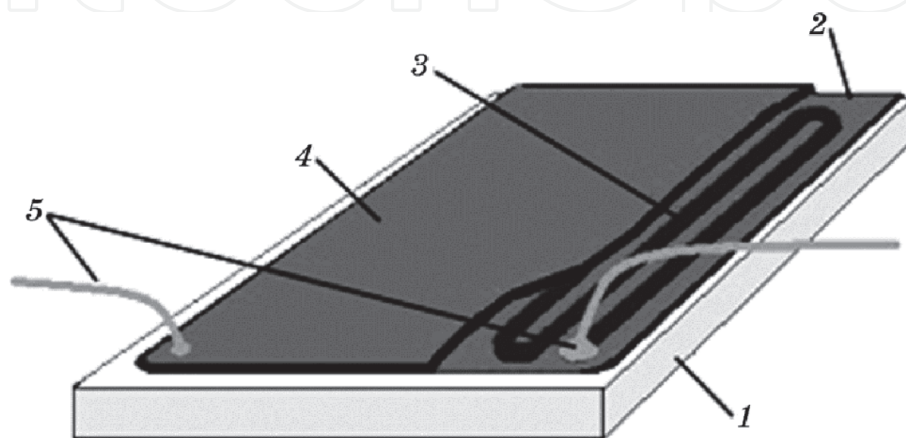


**Figure 1.** Schematic diagram of a film heating element [2]: (1) stainless steel substrate, (2) dielectric layer, (3) resistive element, (4) protective shell, and (5) contact electrodes with current collectors.

| Marking  | Chemical composition, wt% |      |                               |                  |                                |     |
|----------|---------------------------|------|-------------------------------|------------------|--------------------------------|-----|
|          | PbO                       | ZnO  | B <sub>2</sub> O <sub>3</sub> | SiO <sub>2</sub> | Al <sub>2</sub> O <sub>3</sub> | BaO |
| SC 100-1 | 75.5                      | 12.0 | 8.4                           | 2.1              | 2.0                            | –   |
| SC 90-1  | 75.3                      | 11.6 | 8.5                           | 2.1              | 0.8                            | 1.7 |
| SC 88    | 75.1                      | 11.2 | 9.4                           | 1.9              | –                              | 1.9 |
| SC 90    | 75.3                      | 11.6 | 8.5                           | 2.1              | –                              | 2.5 |

**Table 1.**  
*Chemical compositions of powders for the synthesis of the PbO-ZnO-B<sub>2</sub>O<sub>3</sub> glass-ceramic system-based coatings [2].*

at 1180°C. After holding at this temperature for 60 min, the melt was rapidly cooled to form an amorphous structure and prevent crystallization. The dried granules were ground and sieved to obtain powder fractions with a granule average size of not more than 56 µm. On the basis of the powder obtained, a dielectric paste was made, which was applied to a prepared surface of AISI 420 steel samples and dried at 70°C. For all specimens, standard heat treatment [16–20] was performed with two-step annealing at 380 and 440°C and holding at these temperatures for 45 min. The thermal treatment of the coatings was carried out without a protective atmosphere to activate the formation of oxides.

The coatings were applied to the surface of AISI 420 stainless steel. To determine the adhesion properties, the steel surfaces were treated with three different methods, which allowed obtaining different indices of surface roughness: S1, machine grinding; S2, electrolytic etching; S3, manual grinding [3].

Using the method of interference profilometry, surface profilograms of AISI 420 stainless steel substrates were obtained after various surface treatment methods. From the obtained profilograms using the software “Micron-Gamma,” the basic parameters of the roughness of the substrates were calculated, the values of which are given in **Table 2**.

The surface of AISI 420 stainless steel with roughness S1 and S3 is characterized by a nonuniform row structure with gaps and projections of the height of 4.6–5.2 µm (**Figure 2**). The surface of AISI 420 stainless steel with roughness S3 after electrolytic etching has a more uniform structure. The height of the needle projections is uniform and averages 5.3 µm.

Traditional methods do not allow qualitative estimation of quantitative indices of adhesion strength of coatings obtained by the method of thick films, the thickness of which exceeds 100 µm. Because of this, indirect methods of investigation can be used to predict the adhesion strength of such coatings, in particular, the determination of the free surface energy of the substrates on which the coatings are synthesized (**Figure 3**). It is known that the level of surface energy will specify the adhesion properties. This technique allows determining the level of the adhesion

| Marking     | Arithmetical mean deviation of the assessed profile <i>Ra</i> , µm | Average distance based on the ten highest peaks and lowest valleys over the entire sampling length <i>Rz</i> , µm | Maximum height of the profile <i>Rmax</i> , µm | Average step of peaks along the mean line <i>Sm</i> , µm |
|-------------|--|---|--|--|
| AISI 420—S1 | 1.11   | 5.11  | 4.68   | 1.02   |
| AISI 420—S2 | 1.31   | 5.15  | 5.36   | 1.03   |
| AISI 420—S3 | 1.11   | 4.00  | 5.21   | 1.00   |

**Table 2.**  
*Surface roughness parameters of the AISI 420 steel substrates after various types of grinding operations [3].*



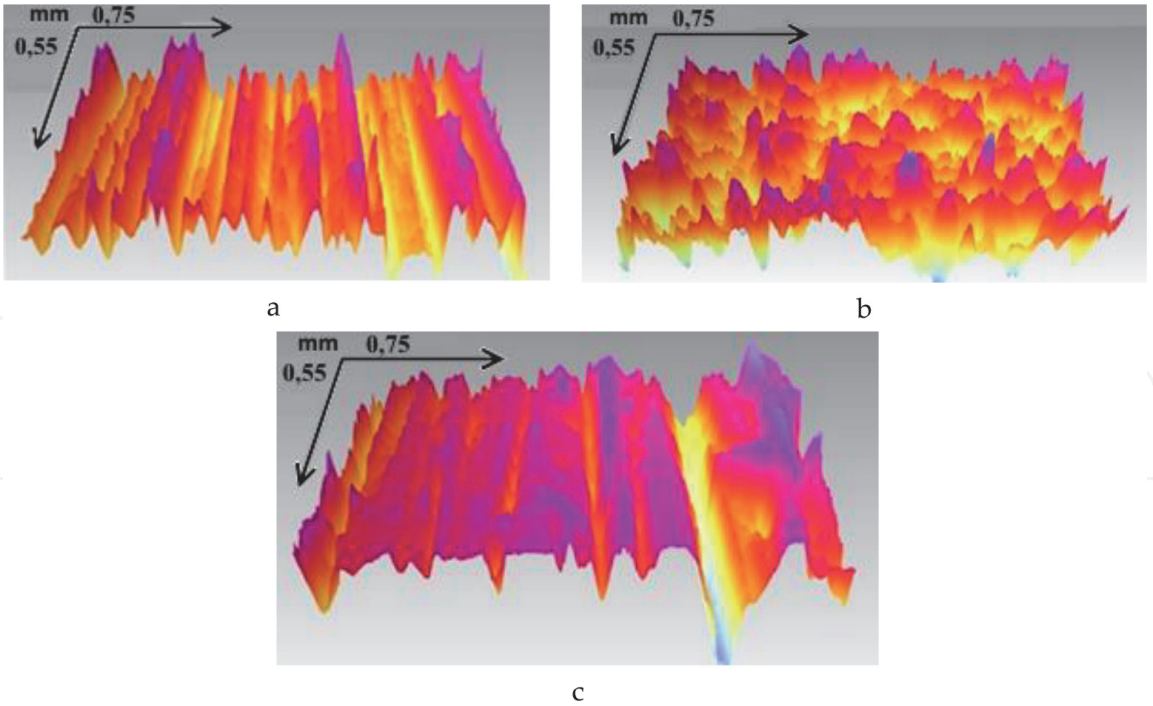


**Figure 2.** Three-dimensional surface microtopography of AISI 420 steel substrates after various types of grinding operations: (a) machine grinding S1; (b) electrolytic etching S2; (c) manual grinding S3 [3].

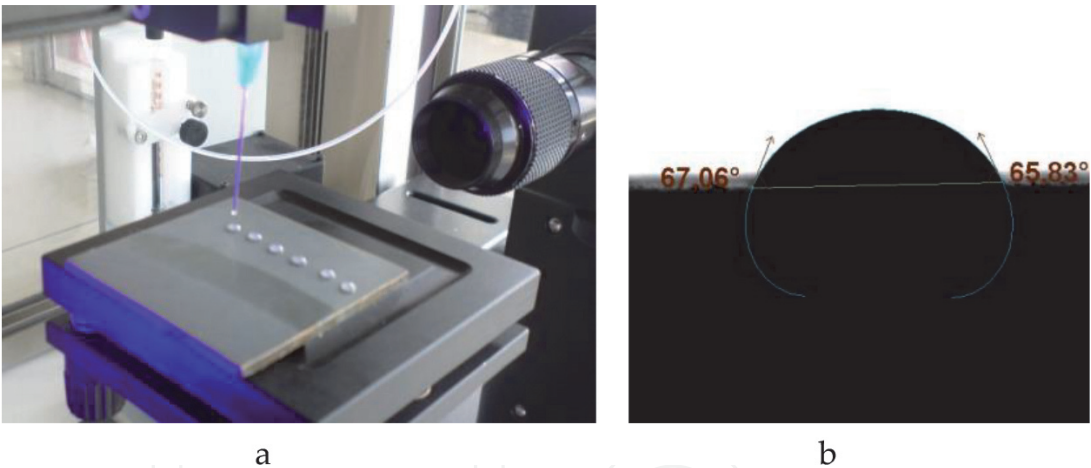


**Figure 3.** General view of the desktop of the KSV Attension Theta optical tensiometer (a) and the droplet along with the calculated wetting angles (b) [3].

strength in the coating-substrate system if the actual contact area between them is known [21–24].

To predict the adhesion strength of the dielectric coating to the substrate, the surface topography of the prepared substrates was investigated, and the values of the free surface energy were calculated for them. Optical tensiometry was used to calculate the free surface energy with the measurement of wetting angles between the test surface and droplets of substances: water, glycerol, formamide, ethylene glycol, diiodomethane, and bromonaphthalene [3]. **Figure 4** shows the change in the wetting angles for the substrates after various surface treatments, depending on the type of drip fraction of the substance applied to the surface.

The substrates S1 and S2 have the highest average values of the wetting angles. This testifies to the dependence of the wetting angle not only on the physicochemical properties of the droplet but also on the roughness and microtopography of the surface.

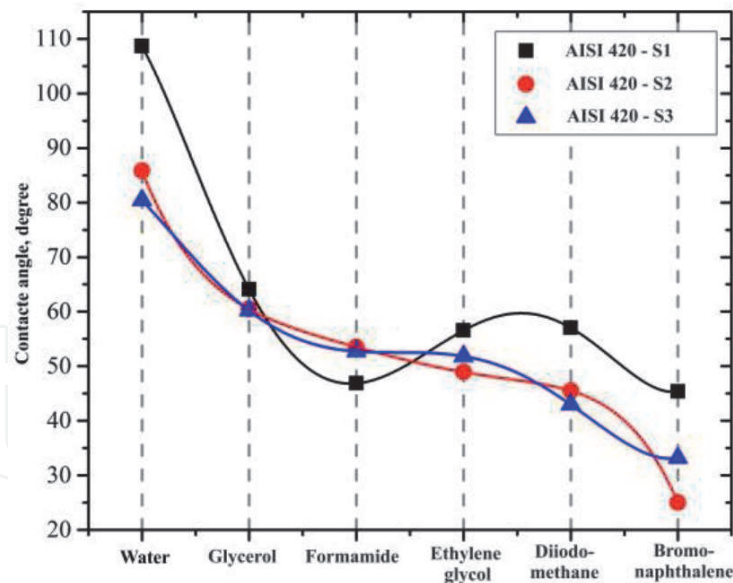


**Figure 4.**  
Values of wetting angles for AISI 420 stainless steel substrates after machine grinding S1, electrolytic etching S2, and manual grinding S3 depending on the substance of the droplet.

By changing the values of the wetting angle using two calculation methods, the values of the free surface energy components for the substrates S1, S2, and S3 were determined (**Table 3**). The first calculation method [25] gave a large variation of the experimental data, which makes it difficult to predict the physical and mechanical properties of the surface being studied. According to the second calculation method [26], the substrates S1 and S2 have the highest values of the free surface energy. This is confirmed by the fact that the actual contact surface area increases with increasing roughness. This, in turn, will increase the free surface energy indices, which will be reflected in the adsorption component of adhesion.

Thus, the formation of the developed surface structure of AISI 420 stainless steel substrates obtained by the surface etching method will provide the maximum level of the free surface energy by forming the largest contact area between the applied dielectric layer and the substrate, which will provide the best level of adhesion uniformity [3].

To obtain a high-quality insulation coating on the surface of stainless steels, it is necessary to ensure the maximum homogeneity of its structure in both the thickness and surface area. The surface roughness of such coatings must be within  $Rz = 1\text{--}2\text{ }\mu\text{m}$  to provide the required adhesion strength between dielectric and resistive

| Constituents of surface energy |          | Lifshitz-van der Waals energy $\gamma^{\text{LW}}$ (mJ/m <sup>2</sup> ) | Energy of the electron acceptors $\gamma^+$ (mJ/m <sup>2</sup> ) | Energy of the electron donors $\gamma^-$ (mJ/m <sup>2</sup> ) | Total surface energy $\gamma^{\text{tot}}$ (mJ/m <sup>2</sup> ) |
|--------------------------------|----------|---|--|---|---|
| S1                             | Method 1 | 32.3  | 0.2  | 2.7   | 34.2  |
|                                | Method 2 | 34.8  | 1.4  | 4.8   | 39.9  |
| S2                             | Method 1 | 39.2  | 1.2  | 0.7   | 41.0  |
|                                | Method 2 | 36.9  | 2.5  | 1.1   | 40.2  |
| S3                             | Method 1 | 38.2  | 2.4  | 0.6   | 40.6  |
|                                | Method 2 | 34.9  | 7.4  | 0.4   | 38.2  |

**Table 3.**  
Values of the free surface energy constituents for the substrates S1, S2, and S3 and coatings based on the PbO-ZnO-B<sub>2</sub>O<sub>3</sub> glass crystalline system [3].

layers. It should be noted that the glass-ceramic coating should have a minimum porosity to obtain perfect electrophysical characteristics, in particular, the breakdown voltage and electrical strength.

After synthesis and heat treatment, the obtained glass-ceramic coatings have a dark gray color with shades of green and are smooth to the touch. Small projections and gaps are observed along the entire area of the formed coating. No defects in the form of pores, gas bubbles, or residues of non-smelted sealant (SC, sital cement) powder have been detected. The thickness of the coatings ranges from 90 to 105  $\mu\text{m}$ .

To evaluate the microgeometry parameters of the surface structure for each synthesized coating, the surface topography was investigated in five sections of the surface with a section area of  $0.55 \times 0.75 \text{ mm}^2$ . Surface profilograms of the coatings were obtained using the interference profilometer (Figure 5).

Structural and geometric parameters of the surface roughness of the coatings, the values of which are given in Table 4, were calculated from the obtained profilograms using the Micron-Gamma software. According to Table 4, the values of  $R_z$  parameter of the surface roughness are 2.11, 1.87, 1.63, and 2.14  $\mu\text{m}$  for the investigated coatings SC 100-1, SC 90-1, SC 88, and SC 90, respectively.

The study of three-dimensional topography of the surface of the formed coatings by the method of interference profilometry testifies to the presence of identical fragments of their structure, regardless of the microtopography of the substrate surface (Figure 6).

Coatings based on powders SC 100-1, SC 90-1, SC 88, and SC 90 have a homogeneous structure with shallow round gaps and needle projections of height 0.8–1.1  $\mu\text{m}$ .

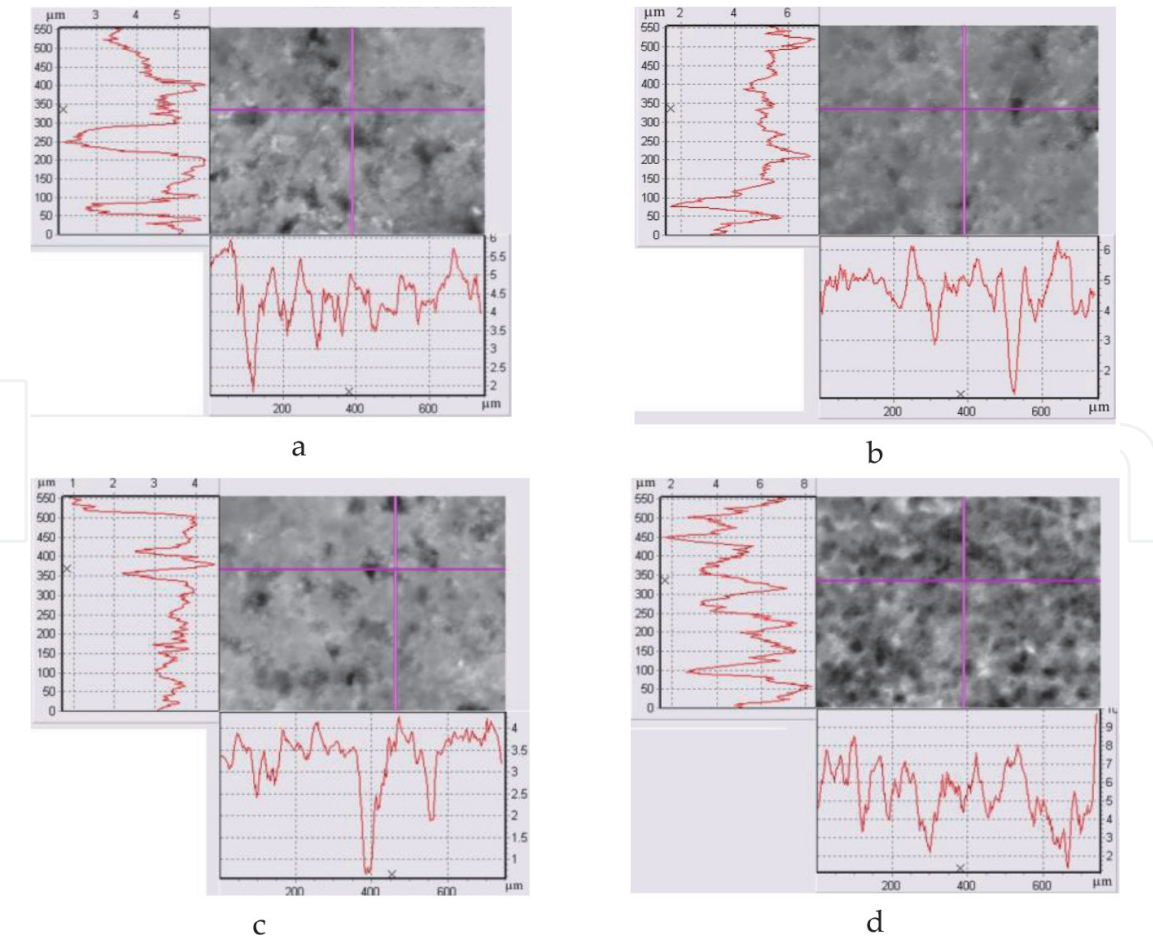


**Figure 5.** Surface profilograms of synthesized functional coatings based on glass crystalline materials of grades (a) SC 100-1, (b) SC 90-1, (c) SC 88, and (d) SC 90 on AISI 420 stainless steel substrates [3].



| Marking  | Arithmetical mean deviation of the assessed profile<br>$R_a, \mu\text{m}$ | Average distance based on the 10 highest peaks and lowest valleys over the entire sampling length<br>$R_z, \mu\text{m}$ | Maximum height of the profile $R_{\text{max}}, \mu\text{m}$ | Average step of peaks along the mean line $S_m, \mu\text{m}$ |
|----------|---|---|---|--|
| SC 100-1 | 0.55  | 2.11  | 2.29  | 1.01   |
| SC 90-1  | 0.49  | 1.87  | 2.21  | 1.01   |
| SC 88    | 0.41  | 1.63  | 1.82  | 1.00   |
| SC 90    | 0.57  | 2.14  | 2.29  | 1.01   |

**Table 4.**  
*Parameters of surface roughness of coatings SC 100-1, SC 90-1, SC 88, and SC 90 [3].*

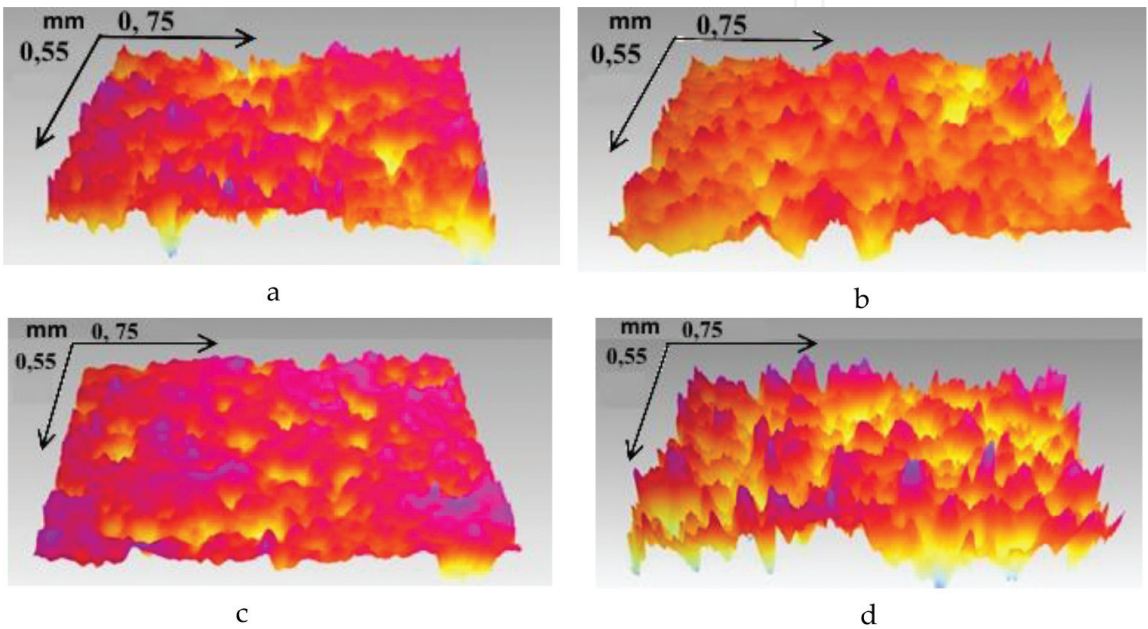


**Figure 6.**  
*Three-dimensional microtopography of the surfaces of functional coatings based on glass crystalline materials of grades (a) SC 100-1, (b) SC 90-1, (c) SC 88, and (d) SC 90 on AISI 420 stainless steel substrates [3].*

Such surface microtopography of the dielectric coating will guarantee correspondingly high adhesion strength of the applied resistive layer [1–3].

**2.1 Microstructure of functional coatings based on glass crystalline materials**

The dendritic component has been revealed in the surface layers of the dielectric coatings using a scanning electron microscope (**Figure 7**). This is a positive feature because it is the crystalline component of the microstructure of the  $\text{PbO-ZnO-B}_2\text{O}_3$  system coating that is responsible for the proper functional properties of the insulation layer [4]. The largest dendritic crystals are observed in the structure of SC 100-1 and SC 90 coatings. As the coatings of SC 100-1 and SC 90 grades have the highest surface roughness compared to the other two coating grades, it can be assumed that the growth rate of dendritic crystals will affect the final surface roughness parameters of the coatings.

It should be noted that the presence of an amorphous phase in the amount of more than 15% will cause a significant deterioration of the micromechanical and thermophysical characteristics of coatings while increasing the dielectric strength [4].



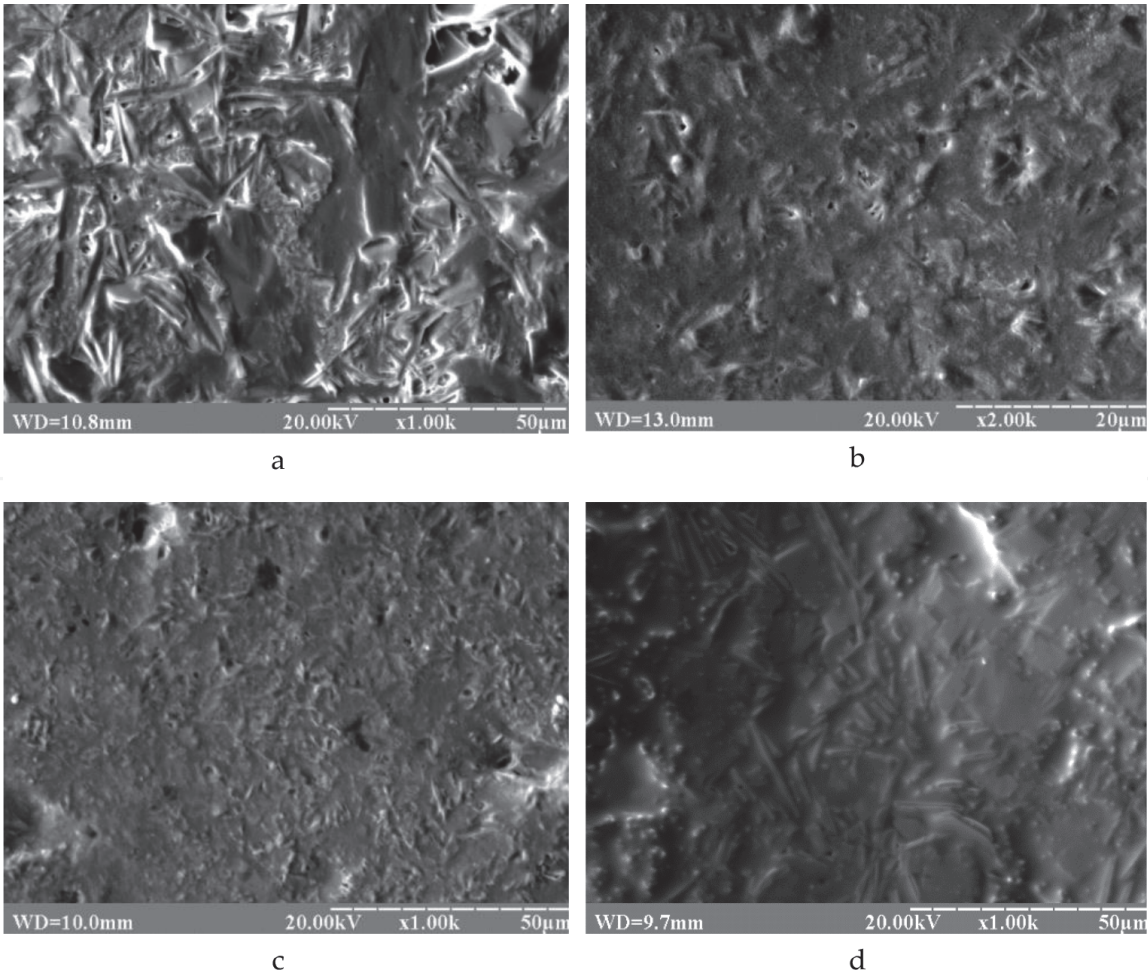


**Figure 7.**  
*Surface microstructure of dielectric coatings based on glass crystalline materials of grades (a) SC 100-1, (b) SC 90-1, (c) SC 88, and (d) SC 90 [4].*

To evaluate the porosity of coatings based on glass crystalline materials of SC 100-1 and SC 90-1 grades, their microstructure after polishing was investigated (**Figure 8**). They are found to contain a large number of pores of different sizes, unevenly distributed in the bulk of the coatings. The formation of pores can be explained by the uncontrolled process of sublimation of organic solvents (butyl acetate, amyl acetate) during synthesis at temperatures of 250–350°C.

Quantitative analysis of the porosity of synthesized coatings based on SC 90-1 and SC 100-1 powders was carried out (**Table 5**). It was found out that the volume

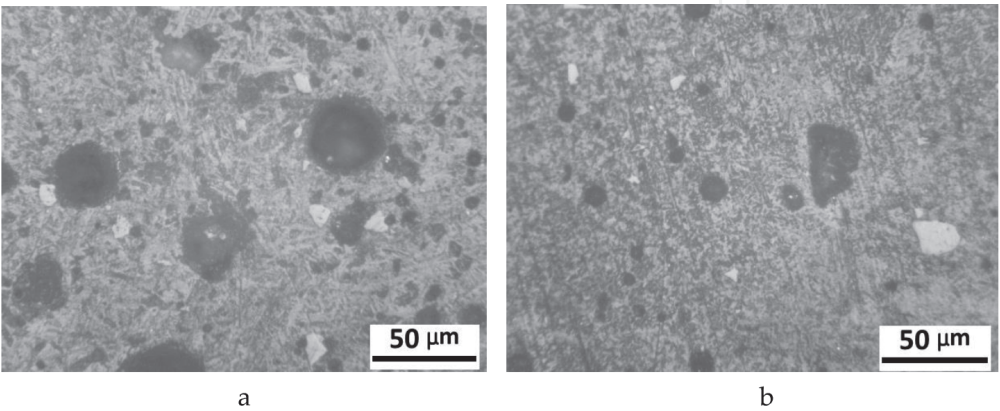


**Figure 8.**  
*The microstructure of coatings based on glass crystalline materials of grades (a) SC 100-1 and (b) SC 90-1 after polishing [4].*

| Parameter                                     | Coating based on SC 90-1 powder | Coating based on SC 100-1 powder |
|---|---------------------------------|----------------------------------|
| Number of pores per field of view             | 157                             | 88                               |
| Volume fraction of pores, %                   | 4.1                             | 19.7                             |
| Specific surface of pores                     | 0.031                           | 0.047                            |
| Mean chord length of pores, $\mu\text{m}$     | 5.3                             | 16.9                             |
| Average distance between pores, $\mu\text{m}$ | 126.5                           | 69.1                             |
| Fractal dimension                             | 1.07                            | 1.56                             |
| Form factor                                   | 0.867                           | 0.825                            |
| Compact factor                                | 0.989                           | 0.935                            |
| Stretching factor                             | 0.815                           | 0.734                            |
| Cutting factor of the contour                 | 0.867                           | 0.859                            |

**Table 5.**  
*Quantitative analysis of the porosity of coatings SC 100-1 and SC 90-1.*

fraction of pores in the structure of the SC 90-1-based glass-ceramic material coating is 4.1%, in contrast to the coating SC 100-1, the average porosity of which is 19.7%.

The difference in the structure of the coatings can be explained by the alloying of the  $\text{PbO-ZnO-B}_2\text{O}_3$  system with BaO oxide in quantities up to 1.7%, which reduces the temperature of formation of the amorphous glass material in the synthesis stage, which in turn causes acceleration of the sublimation processes of organic solvents and accelerates the crystallization process [4].

The microstructural analysis of the polished transverse sections of the synthesized coatings on AISI 420 steel substrates was carried out. Using energy dispersive X-ray spectroscopy (EDS), it was found that no diffusion or transition zones are formed between the applied coatings and the substrates. This is evidenced by a sharp drop in the content of lead in the place where the coating is bonded to the substrate (**Figure 9**). This indicates a significant influence of electrochemical processes (double electric layer) during the formation of a strong adhesion of the synthesized glass crystalline coatings of the  $\text{PbO-ZnO-B}_2\text{O}_3$  system with the substrate surfaces.

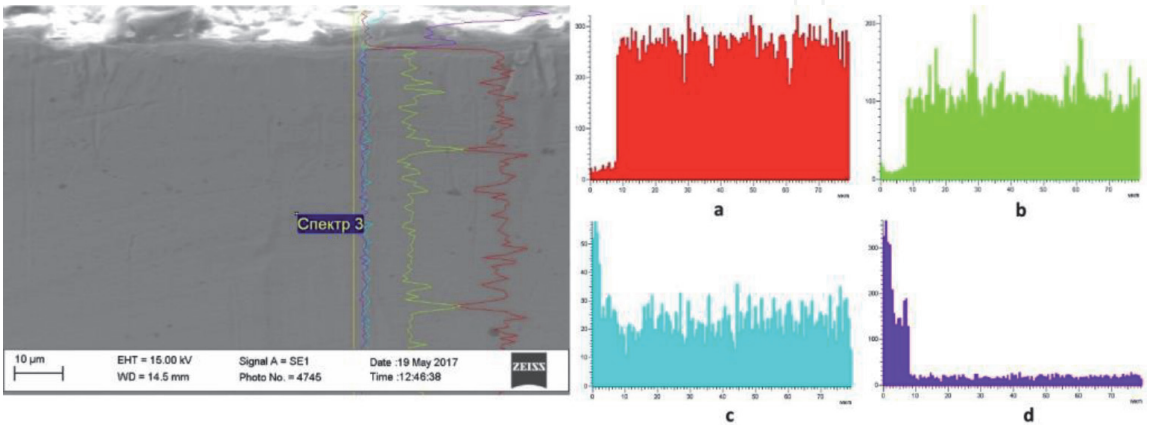


**Figure 9.**  
*The local EDS microanalysis of the coating based on the glass crystalline material of SC 90-1 grade by the depth of the layer showing the distribution of elements (a) Fe, (b) Cr, (c) Si, and (d) Pb.*

## 2.2 X-ray structural studies of functional coatings based on glass crystalline materials

The diffraction pattern of the coating based on the SC 100-1 powder (**Figure 10**) confirms the fact of the formation of a crystalline structure during synthesis. It shows pronounced peaks corresponding to lead and zinc as pure chemical elements. The shape and height of the peaks indicate the presence of crystalline phases in the volume of the coating.

To determine the chemical homogeneity of the coatings, a local EDS micro-analysis was performed. It was detected lead, zinc, and boron oxides in all types of synthesized coatings in various proportions depending on the location of the analysis.

In the coatings based on SC 90-1, SC 88, and SC 90 powders, BaO and SiO<sub>2</sub> oxides were found. Due to the low accuracy of the EDS method when detecting light elements, including boron oxide, the volume fraction of each of the oxides in the coating structure could not be estimated correctly.

X-ray photoelectron spectroscopy (XPS) was used to determine the qualitative and quantitative chemical composition of coatings, as it allows doing this more accurately and detecting all chemical elements except hydrogen and helium. This technique is based on obtaining XPS spectra by irradiating a material with a beam of X-rays (Al K $\alpha$ ) while simultaneously measuring the kinetic energy and number of electrons that escape from the top 0 to 10 nm of the coating being analyzed. To improve the reliability of the results obtained, the evaluation of the chemical composition was performed in three different areas on the sample surfaces. According to the investigation results, experimental diffraction patterns were constructed (**Figure 11**).

It was revealed that the elemental compositions of the synthesized coatings correspond to the compositions of the original powders within the error of the device (2%). As an example, the chemical composition of the synthesized coating based on sital cement of SC 90-1 grade is as follows: 75.3 wt% PbO, 11.6 wt% ZnO, 8.5 wt% B<sub>2</sub>O<sub>3</sub>, 2.1 wt% SiO<sub>2</sub>, 0.8 wt% Al<sub>2</sub>O<sub>3</sub>, and 1.7 wt% BaO. Besides, unwanted phases of 0.15% BaSO<sub>4</sub>, 1.02 % (ZnS + ZnF<sub>2</sub>), and 0.28% B<sub>4</sub>C, which could be formed during prolonged isothermal holding and interaction of powder particles with residues of nitrocellulose lacquer, were detected. To avoid the formation of these phases, it is necessary to increase the annealing temperature to accelerate the crystallization process and simultaneously reduce the holding time. However, it

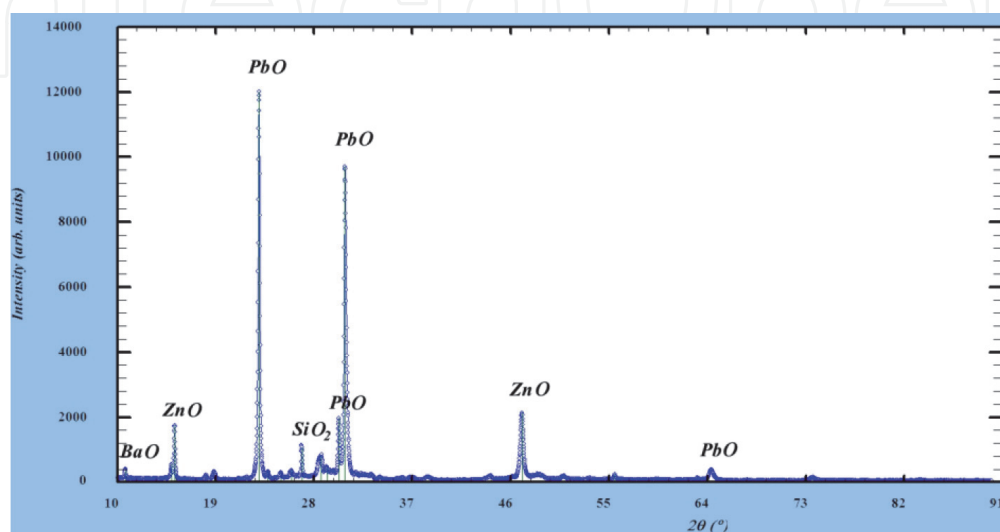


**Figure 10.**

*X-ray pattern of the surface of the coating based on the glass crystalline material of SC 100-1 grade.*



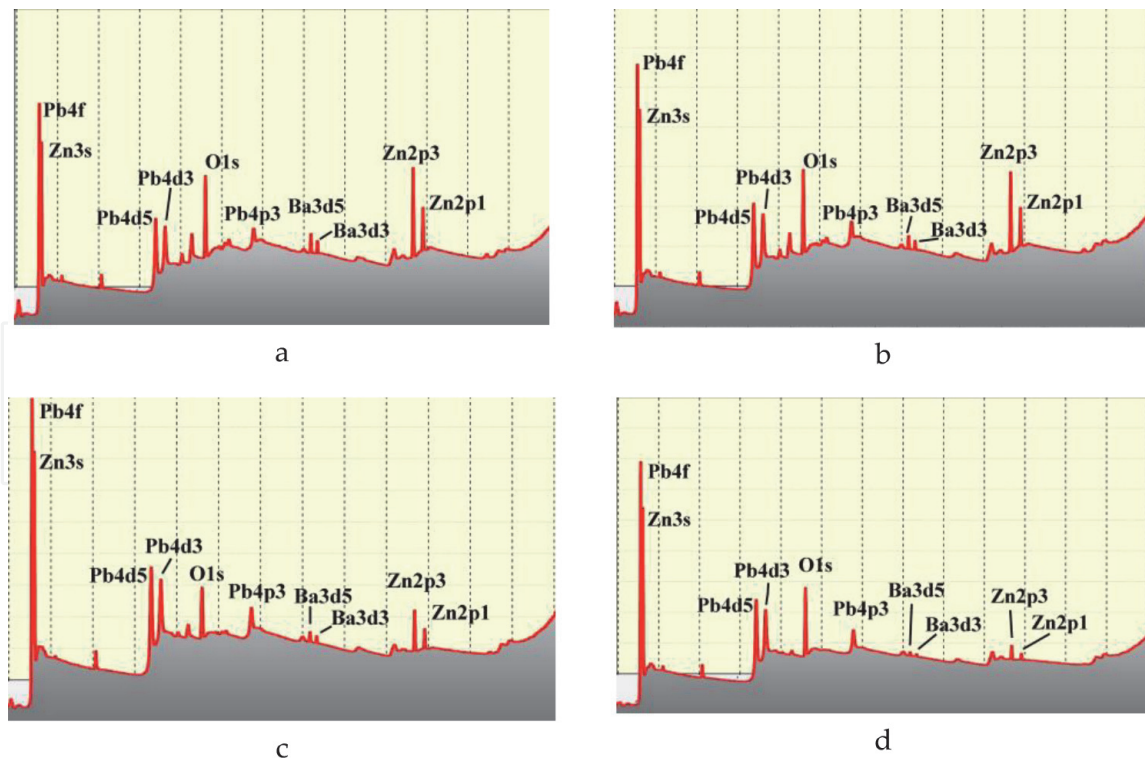


**Figure 11.**  
*Experimental X-ray patterns of the surfaces of coatings based on glass crystalline materials of grades (a) SC 100-1, (b) SC 90-1, (c) SC 88, and (d) SC 90 obtained by X-ray photoelectron spectroscopy.*

should be remembered that the final crystallization temperature should not exceed the glass spill temperature more than two times (in our case up to 520°C).

### 3. Formation of insulating coatings by plasma chemical vapor deposition (CVD)

The ion-plasma sputtering as one of the CVD technique methods was chosen as an alternative method of synthesizing protective insulating coatings on stainless steels. As materials for the sputtering, it is advisable to use pure compounds based on nitrides and oxides of metals, which have a wide range of functional properties [27–31].

The most optimal materials for application to the surfaces of ferritic and ferritic-martensitic stainless steels are coatings of magnesia (MgO), alumina (Al<sub>2</sub>O<sub>3</sub>), titanium dioxide (TiO<sub>2</sub>), and aluminum nitride (AlN) (**Table 6**). It should be noted that the thermal conductivity of beryllium oxide (BeO) is nine times higher than of the listed materials. Thus, it can significantly increase the power of FHE on stainless steel substrates. However, the use of BeO is hampered by its high cost and toxicity during processing. Traditionally, this or that type of ceramics is obtained by sintering oxide or nitride powders at various temperatures. However, high-energy methods of surface engineering are promising when forming dielectric layers on the surfaces of various structural materials. The properties of the layers synthesized in this way, which are given in various literary sources, differ significantly and depend on a method used to form these layers.

Magnesium oxide is the only oxygen compound of magnesium. It exists in only one modification and crystallizes in a cubic system. The crystalline form of MgO is called periclase. It has a potassium salt lattice with a parameter of 0.42 nm. By its chemical properties, MgO is a basic oxide, and, as a consequence, it combines with



| Parameter   | MgO                  | AlN  | Al <sub>2</sub> O <sub>3</sub>                              | TiO <sub>2</sub>              |
|---|----------------------|--|---|-------------------------------|
| Density, g/cm <sup>3</sup>  | 3.58                 | 3.2–3.24   | 3.6   | 3.9–4.3                       |
| Dielectric constant   | 8–9                  | 8.5  | 12.0  | 31–173 (114 for rutile)       |
| Relative density  | 0.95–0.96            | 0.96–0.98  | 0.94–0.98   | -                             |
| Melting point, °C   | 2800                 | 2400   | 2050  | 1855                          |
| Operating temperature range for an atmosphere, °C                               | Up to 2000 in air    | 1300–1400  | 1600–1700   | -                             |
| Sintering temperature, °C   | 1600                 | -  | 1700–1750   | -                             |
| Coefficient of linear thermal expansion $\alpha$ , $\times 10^6 \text{ K}^{-1}$ | 11.7–14.2            | 4.8  | 5–6.7   | 9.8–10.8                      |
| Thermal conductivity, $\text{W m}^{-1} \text{ K}^{-1}$                          | 28.0                 | 66   | 24–29   |                               |
| Modification  | Cubic<br>a = 0.42 nm | Hexagonal<br>a = 0.31–0.313 nm<br>c = 0.493–0.498 nm | $\alpha$ -Trigonal<br>$\beta$ -Hexagonal<br>$\gamma$ -Cubic | Anatase<br>Brookite<br>Rutile |

**Table 6.**  
*Physical properties of materials of the dielectric layer.*

all acidic oxides and dissolves in inorganic acids (partially in water). Hydration of MgO limits the possibility of its fine fragmentation in water, as it increases greatly with increasing both fragmentation and temperature. MgO sintering is facilitated by TiO<sub>2</sub>, ZrO<sub>2</sub>, Al<sub>2</sub>O<sub>3</sub>, and Fe<sub>2</sub>O<sub>3</sub> impurities. Magnesium oxide is a good insulator. Its crystals have ionic conductivity. The work [32] presents the study of the electrical properties of magnesium oxide layers formed by magnetron sputtering of magnesium followed by annealing in air. It is found out that, depending on the annealing temperature, the layer resistivity ranges from  $1.7 \times 10^7$  to  $2.81 \times 10^{12}$  mOhm cm. The work [33] presents the study of MgO layers formed by the sol-gel method. The obtained results indicate the weak crystallinity and the disorientation of the magnesium oxide phase. The breakdown voltage ranges from 5 to 78 MW/cm. Leakage currents when heated to 250°C increase within  $10^{-9}$ – $10^{-3}$  A/cm<sup>2</sup>. In the work [34], using the method of pulsed laser deposition, MgO polycrystalline films with various crystallographic orientations were obtained. The value of the dielectric constant was 9.67 for a density near the band gap of  $4.5 \times 10^{11} \text{ eV}^{-1} \text{ cm}^{-2}$ . In some works [32–35], magnesia ceramics are characterized by a dense fine-crystalline structure with perfect physical, mechanical, and electrophysical properties.

Another promising material widely used in radio and microelectronic technology is aluminum oxide [33–35]. It is known for its nine crystallographic modifications, the most important for the industry being  $\alpha$ -modification. The corundum structure (**Figure 12**) can be considered as a hexagonal dense packing of O<sup>2-</sup> ions in which 2/3 of the octahedral gaps are occupied by Al<sup>3+</sup>.

The sintering temperature of  $\alpha$ -Al<sub>2</sub>O<sub>3</sub> of technical purity (99–99.5) and the fraction grade of 1–2  $\mu\text{m}$  without additives are 1700–1750°C. At this temperature, a density of 3.75–3.85 g/cm<sup>3</sup> is reached. The porosity of the sintered corundum is mainly closed and internal, and the pore shape is circular. The size of initial Al<sub>2</sub>O<sub>3</sub> particles has a decisive influence on the sintering temperature. The maximum size of Al<sub>2</sub>O<sub>3</sub> crystallites capable of active solid phase sintering should not exceed 3–5  $\mu\text{m}$ . By adding to Al<sub>2</sub>O<sub>3</sub> powder some substances in the form of oxides or salts called mineralizers, it is possible to reduce the sintering temperature of corundum by 150–200°C, and the character of crystallization can become directional because the delay or growth of crystals in certain directions is ensured. Among the additives

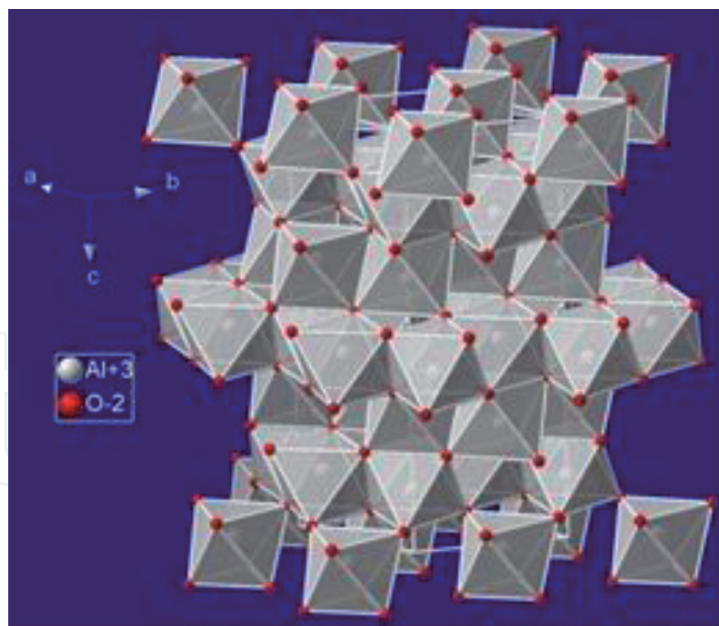


**Figure 12.**  
 Coordination polyhedra in  $\alpha$ - $\text{Al}_2\text{O}_3$  structure [36].

that delay the growth of crystals, the oxides  $\text{TiO}_2$ ,  $\text{MnO}_2$ , and  $\text{Fe}_2\text{O}_3$  should be noted. The most effective is the addition of  $\text{TiO}_2$ , forming a solid solution and reducing the sintering temperature of corundum to 1500–1550°C. The introduction of the  $\text{Mn}^{4+}$  ion, whose ion radius is 0.052 nm, should also lead to the formation of an interstitial solid solution. Another group of additives affects the growth of crystals during annealing. The addition of such compounds results in crystal growth, sometimes very intense, and the sintering temperature can either decrease or remain unchanged. Thus, there are additives that simultaneously reduce the sintering temperature and affect the growth of crystals.

The formation of coatings has many technological difficulties related to the provision of the required stoichiometry, phase composition, crystalline structure, impurity level, porosity, etc. In the work [5], the influence of the parameters of the  $\text{Al}_2\text{O}_3$  film forming process in high-frequency magnetron discharge on the structure, phase composition, porosity, and electrical strength of the films was investigated. It is shown that under appropriate conditions, multiphase polycrystalline coatings with stable  $\alpha$ -structure are formed. Their electrical strength varies in the range of 0.4–1.6 V/m. The high chemical and thermal resistances of aluminum oxide make it possible to use it in the manufacture of heating devices.

Aluminum nitride is the only compound of nitrogen with aluminum that has high chemical resistance. It crystallizes to form a hexagonal lattice of the wurtzite type with parameters  $a = 0.31\text{--}0.313$  nm and  $c = 0.493\text{--}0.498$  nm. Aluminum nitride has no modification, which simplifies the technology of manufacturing products. At 1900–2000°C, AlN decomposes. AlN ceramics can be used in an inert environment up to 1800°C, in vacuum up to 1600°C, in air up to 1300–1400°C. The high thermal conductivity ( $140\text{--}280$  W  $\text{m}^{-1}$   $\text{K}^{-1}$ ), which is a characteristic of aluminum nitride, and the heat resistance make these ceramics promising for use in conditions with a sharp change in temperature. In particular, the thermophysical properties of aluminum nitride ceramics were investigated in. The heat capacity of  $C_p$  was measured using the standard adiabatic calorimeter method. The thermal conductivity  $\chi$  was determined by the absolute stationary longitudinal heat flux method. It was found that at room temperature  $C_p = 25$  J  $\text{mol}^{-1}$   $\text{K}^{-1}$ ,  $\chi = 123$  W  $\text{m}^{-1}$   $\text{K}^{-1}$ . The CLTE was  $(2.9\text{--}3.4) \times 10^{-6}$   $\text{K}^{-1}$ . Aluminum nitride has also been used as a protective coating

for electronic components under the influence of percussion mechanical loads, which is associated with its high hardness (7–8 on the Mohs scale) [2, 5].

Ceramics, the crystalline base of which is titanium dioxide, are considered as a separate grade of technical ceramics since this compound has a high value of relative permittivity as compared to other ceramic materials (**Table 6**). Titanium oxide films, due to their physicochemical properties, are widely used as protective and optically sensitive coatings in gas sensors and during photocatalysis. They are also used in microelectronics (dynamic memory, field-effect transistors, ferromagnetic materials). Besides,  $\text{TiO}_2$  is used in electronic engineering, in particular for the manufacture of capacitors. Titanium dioxide does not occur in nature in pure form. It is obtained by chemical processing of titanium ores  $\text{FeTiO}_3$ ,  $\text{CaTiSiO}_5$ ,  $\text{CaTiO}_3$ , and others. Titanium dioxide is available in three modifications: anatase, brookite, and rutile. Rutile is a stable high-temperature form of titanium dioxide, and the other two transforms irreversibly into this. Anatase modification of titanium dioxide is used as a catalyst and component of solar cells. Due to its high reflectance, it is used to protect spacecraft from the sun's radiation. For the ceramics industry, they produce a special brand of  $\text{TiO}_2$  called "capacitor."

Thus, the properties of  $\text{MgO}$ ,  $\text{Al}_2\text{O}_3$ ,  $\text{TiO}_2$ , and  $\text{AlN}$  ceramics depend strongly on the method of their production and a set of certain parameters of the initial powders. Of the four dielectric materials presented, all to a greater or lesser extent satisfy the requirements relating to insulating layers of film heating elements based on a stainless steel substrate. Thus, titanium oxide has high relative permittivity, while aluminum nitride has high thermal conductivity. Both magnesium and aluminum oxides have satisfactory electrical strength at low CLTE. The combination of such dielectric properties with the verified technology of forming ceramic coatings on the surfaces of structural materials can serve effectively for the replacement of FHE constituents.

Among the high-energy surface engineering technologies, the ion-plasma sputtering method is the most promising for the formation of dielectric and resistive layers on the surfaces of stainless steels [37]. Therefore, the functional layers were formed by this method using a multifunctional ion-plasma discharge system. To create the dielectric layer by ion-plasma sputtering, a number of materials were analyzed that would provide the dielectric properties of the FHE and meet technological, economic, and environmental requirements. Oxides and nitrides of Mg, Ti, and Al, which corresponded to the abovementioned dielectric properties of FHEs [38], were selected for the application.

The stainless steel substrates were placed in the substrate holder of a reaction chamber at a distance of 40–50 cm from the cathode. The cathodes were made of aluminum of A1 99.7 grade (for  $\text{AlN}$  and  $\text{Al}_2\text{O}_3$ ), magnesium of Mg 98 grade (for  $\text{MgO}$ ), titanium of VT1-00 grade (for  $\text{TiO}_2$ ), and Cr20Ni80-H nichrome alloy (for the resistive layer). They were manufactured in the form of rods with a diameter of 40 mm. The sputtering was performed under various modes in oxygen, nitrogen, or vacuum atmosphere. Each mode was characterized by certain parameters such as the gas pressure in the reaction chamber, the substrate potential, the current, and the sputtering time. To increase the adhesion strength of the layer, the substrate was heated using a furnace placed directly in the reaction chamber of the ion-plasma device. The plasma stream was directed from the cathode region toward the substrate. The beam divergence angle was about  $20^\circ$ . This provided optimum ion density in the plasma stream [37].

After the samples are uploaded, the reaction chamber of the hybrid ion-plasma device was evacuated. Then, using the helicon source in column mode, the final purification of the substrates in an argon plasma stream for 30 min at a pressure of 0.93 Pa, the potential on the substrate  $E = -100$  V, and the current on the sample of

0.15 A was performed. During the purification, argon ions bombarded the substrate, removing residues of contaminants and impurities from its surface [1, 5].

The ion-plasma discharge device is designed to form nanoscale structure elements [32–37] and, due to its low operating temperatures, allows to apply functional layers to virtually any substrate (metal, plastic, ceramics, etc.). The plasma discharge chamber consists of three process modules (helicon source discharge chamber, drift chamber, treatment chamber), which are connected by flanges using vacuum seals. The scheme of the discharge plasma chamber is shown in **Figure 13**. A working chamber is connected directly to a flange of the vacuum system. A table with the substrate is located in this chamber. A drift chamber with docked vacuum arc accelerators is located above the working chamber. The drift chamber is connected to the helicon source discharge camera. Its top is covered by quartz glass, through which high-frequency energy is supplied during discharge using an antenna connected via a coordination unit to a high-frequency generator.

The magnetic coil located in the working chamber provides the plasma stream from the helicon source to the substrate. Besides, it makes it possible to direct the plasma stream from the plasma-arc accelerator toward the substrate, which significantly reduces the amount of transferred micro-droplet fraction that is formed when working with fusible materials ( $T_m < 2000\text{ K}$ ).

For the formation of high-quality insulating and resistive layers, it is necessary to constantly monitor the state of the substrate surface in all stages of the technological process. Only in this case can the reproduction of the results, the stability of the process, and the high level of quality of coatings on the surfaces of stainless steels be ensured. When using standard high-vacuum equipment, the surface of the substrate always contains several adsorbed monolayers with residual components of the atmosphere. A plasma helicon source and plasma-arc accelerators ensure constant action of an argon ion flux on the substrate in all stages of the process. In this case, the density and energy of the ion flux are sufficient to effectively remove the adsorbed light residual components of the atmosphere from the substrate surface

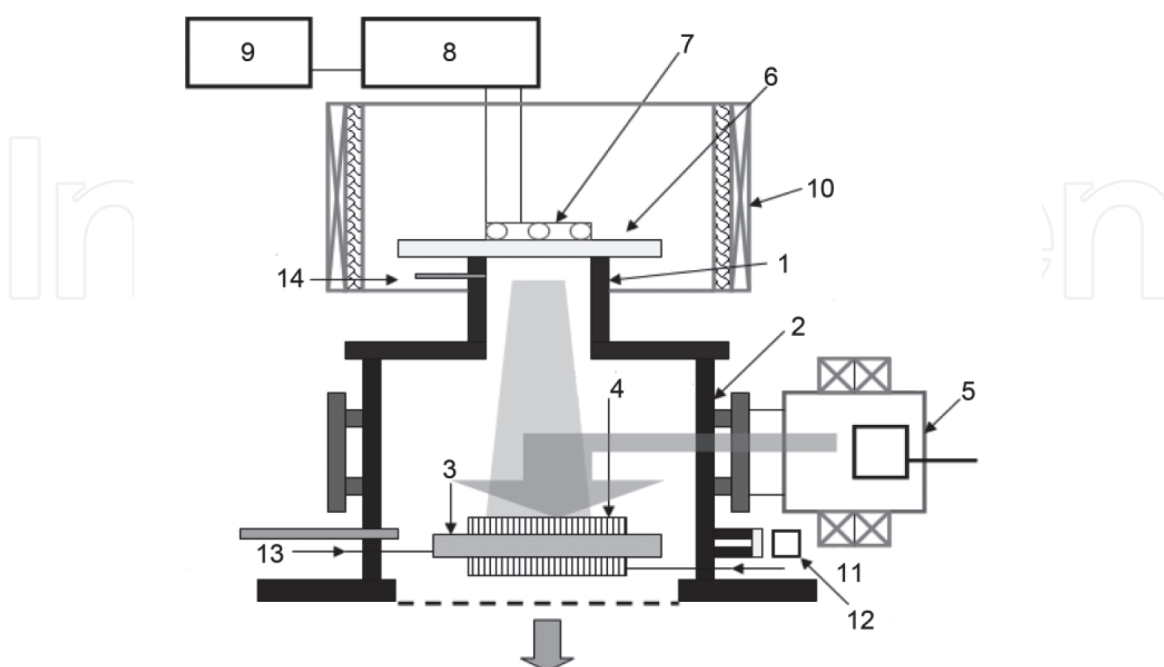


**Figure 13.**

The scheme of the ion-plasma discharge chamber [2, 37]: (1) discharge chamber, (2) drift chamber, (3) table, (4) substrate, (5) plasma-arc accelerator, (6) dielectric window, (7) antenna, (8) coordination unit, (9) HF generator, (10) permanent magnet or an electromagnet, (11) heating system, (12) optical spectrometer, (13) displacement probe, and (14) gas inlet.



layer by the selective sputtering mechanism and do not interfere with the basic technological operations [37].

The ion-plasma device consists of a high-frequency plasma source based on helicon discharge, for the implementation of the CVD process, and plasma-arc accelerators. The high degree of ionization of the plasma stream (more than 80 %) formed by the plasma-arc accelerator allows controlling the thickness of the layers during their application by the value of the total charge transferred to the substrate. **Figure 14** shows a general view of the discharge chamber of an ion-plasma device [2, 37].

Plasma helicon sources are non-electrode high-frequency induction magnetic field sources capable of generating dense ( $n = 10^{11} - 10^{13} \text{ cm}^{-3}$ ) low-temperature ( $T_e = 2 - 10 \text{ eV}$ ) plasma over wide ranges of the operating gas pressure ( $P = 0.5 - 100 \text{ mTorr}$ ) and magnetic fields ( $B = 10 - 2000 \text{ Hs}$ ). These sources range in size from a few centimeters to several meters. They are excited by simple antennas over a wide frequency range ( $f = 7 - 100 \text{ MHz}$ ) and effectively generate plasma at relatively low specific HF power ( $P_{rf} \geq 50 - 100 \text{ mW/cm}^{-3}$ ) [37].

In general, this method is not effective in applying dielectric and resistive layers under conditions of mass production of FHEs, because of the high cost of the device for magnetron sputtering; the small size of the camera, which does not allow sputtering on a large number of samples simultaneously; and the lack of quality cleaning of the working chamber when replacing sputtering cathodes ( $\text{MgO}$ ,  $\text{Al}_2\text{O}_3$ , nichrome, etc.). The application of this method is also limited since the obtained dielectric layers have a high porosity, which increases the probability of electrical breakdown of the coating and failure of the heating device as a whole.

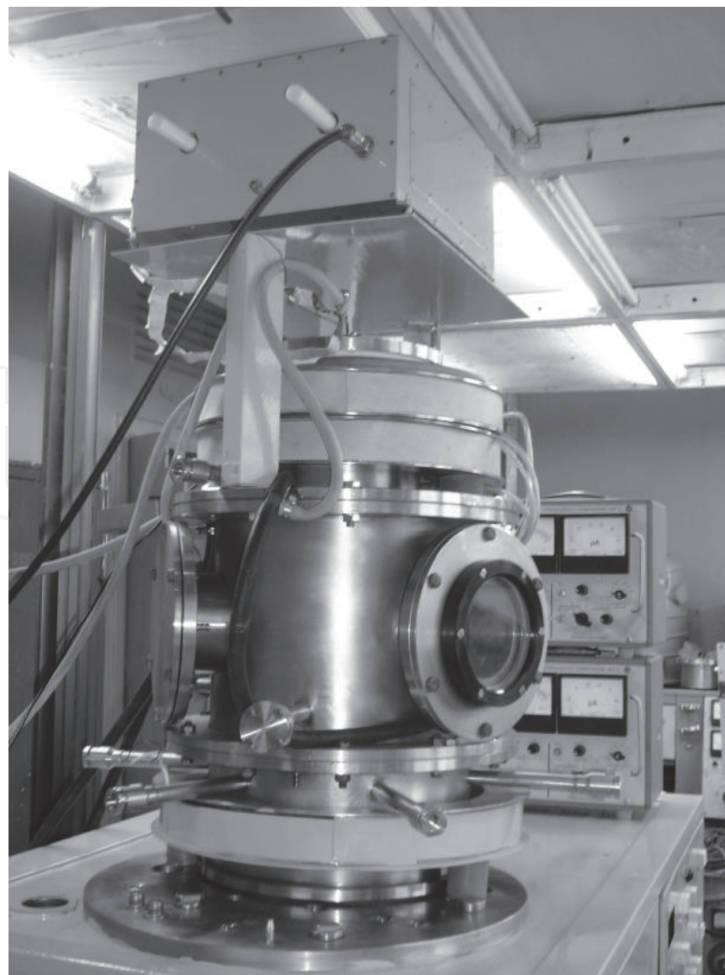


**Figure 14.**  
*General view of the discharge chamber of an ion-plasma device [2].*

Functional dielectric coatings based on oxides of Mg, Ti, and Al for FHEs on stainless steels were obtained by ion-plasma sputtering and were investigated by various methods, namely:

- Study of peculiarities of formation of structure and phase composition of dielectric layers
- Study of adhesion and micromechanical properties
- Measurement of electrophysical characteristics of functional layers

The study of the surface morphology of the formed layers was carried out using an electron microscope JSM-6490LV (JEOL, Japan), equipped with an analytical setup for elemental analysis (spectrometer with energy dispersion INCA Energy+Oxford). Determination of thickness and the structure and elemental composition analyses were performed using a scanning electron microscope with a PEMMA-102-02 microanalyzer. Surface topography was investigated using a Solver P47-PRO atomic force microscope.

The surface morphology of the formed dielectric layer with MgO is shown in **Figure 15**. The grain sizes varied from 20 to 70 nm. Grain growth is likely carried out by an islet mechanism when the formed grain becomes the basis for the formation of nuclei of grains and their subsequent growth (**Figure 15a**). Thus, the newly formed grains are combined into clusters of various sizes. Due to the specific structure, the grains are characterized by a large specific surface, which increases because of petals formed in the perpendicular direction (**Figure 15b**). The thickness of the identified petals is in the range of 10–20 nm. This mechanism of the layer structure formation and a significant difference between the sizes of the grain clusters cause a substantially high porosity of the dielectric layer, which can significantly increase its hygroscopicity [1].

To study the microtopography of the TiO<sub>2</sub> layer surface, SEM and local EDS analyses were performed (**Figure 16**). The surface of the formed layer is continuous and homogeneous, with a small porosity. In some parts of the surface layer, elliptical inclusions of size from 0.08 to 1 μm are observed (**Figure 16b**). Elemental analysis indicates that the bulk of the layer contains titanium and oxygen, the quantitative ratio of which corresponds to the TiO<sub>2</sub> compound of stoichiometric composition. Besides, impurity atoms of iron and aluminum were identified, the presence of which was caused by contamination [2].

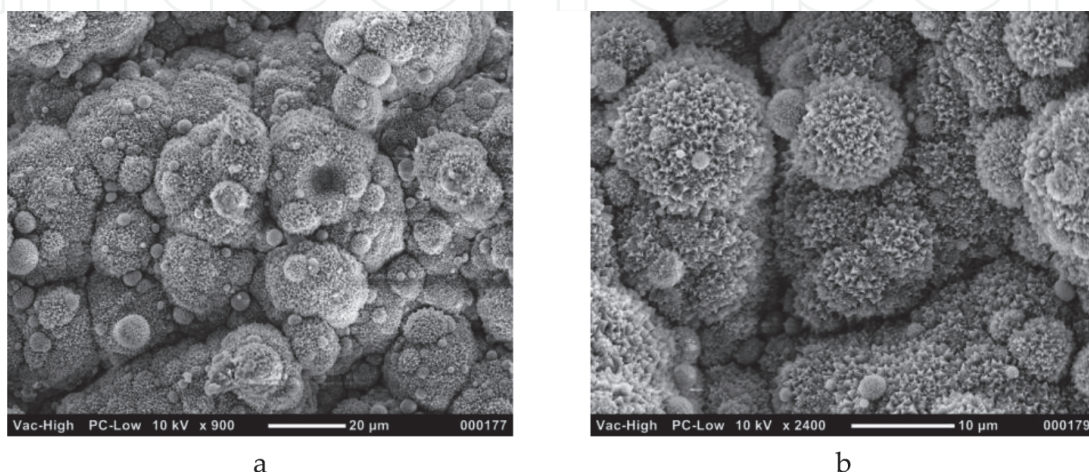


**Figure 15.**  
 SEM surface microtopography of the MgO dielectric layer [2]. Magnifications: (a) 900× and (b) 2400×.



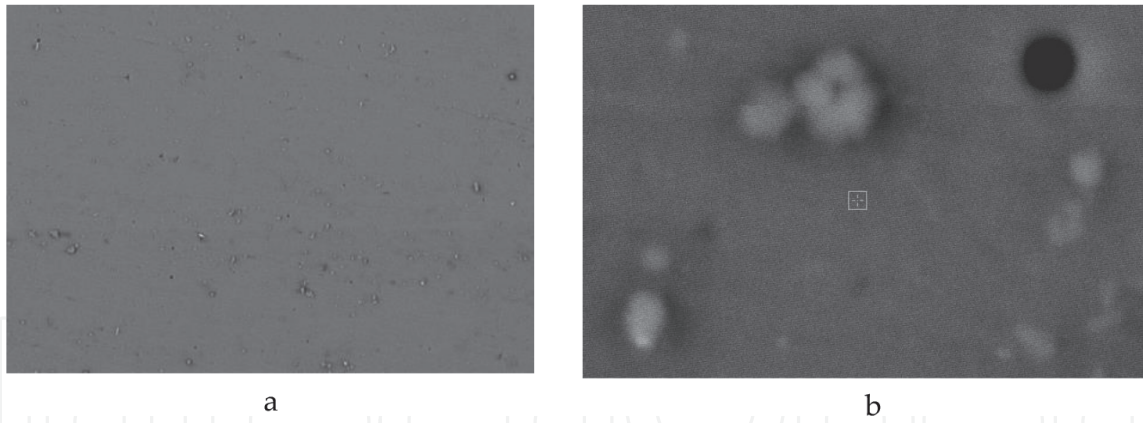


**Figure 16.** SEM surface microtopography of the  $\text{TiO}_2$  dielectric layer [2]. Magnifications: (a)  $900\times$  and (b)  $2400\times$ .

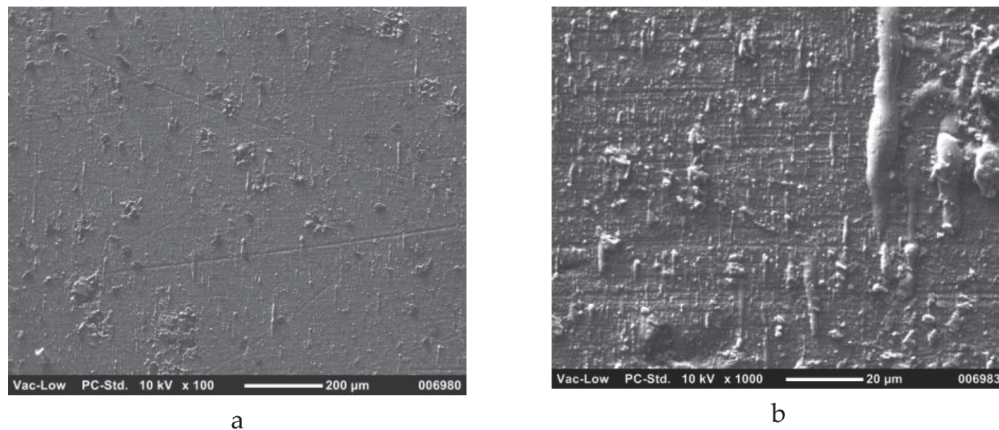


**Figure 17.** SEM surface microtopography of the  $\text{Al}_2\text{O}_3$  dielectric layer [2]. Magnifications: (a)  $100\times$  and (b)  $1000\times$ .

The  $\text{Al}_2\text{O}_3$  layer was formed by ion-plasma deposition of aluminum onto a substrate of the AMg2 aluminum magnesium alloy in an oxygen atmosphere [5]. The result is a layer with a solid, smooth, visually nonporous surface topography (**Figure 17a**). The predominant orientation of individual elements of the surface structure in the form of projections of elongated shape was observed (**Figure 17b**) [1].

By studying SEM microstructure of polished transverse microsections by the depth of the oxide layers  $\text{MgO}$ ,  $\text{TiO}_2$ , and  $\text{Al}_2\text{O}_3$ , it was revealed that all the layers except  $\text{MgO}$  have a gradient structure and consist of two sublayers (**Figure 18**). The inner  $\text{Al}_2\text{O}_3$  sublayer, 1.5–2.5  $\mu\text{m}$  thick, is the boundary section of the substrate layer system and has a highly dispersed structure with a grain size of 90–200 nm, and the outer  $\text{Al}_2\text{O}_3$  sublayer of a thickness of 12.5–13.5  $\mu\text{m}$  has a fragmented structure (**Figure 18a**). The outer  $\text{TiO}_2$  sublayer, 12–13  $\mu\text{m}$  thick, is almost defect-free, uniform, solid, and homogeneous (**Figure 18b**). It has a two-phase structure, with dispersed inclusions of a globular shape, which may belong to one of the  $\text{TiO}_2$  modifications. The inner  $\text{TiO}_2$  sublayer, 2–3  $\mu\text{m}$  thick, adjoins the substrate surface and completely reproduces its morphology. By studying SEM microstructure of polished transverse microsections of  $\text{MgO}$  dielectric layers, it was revealed that their thickness ranges within 25–65  $\mu\text{m}$ .  $\text{MgO}$  layer continuity disturbances were observed only along the boundaries of the separation of large clusters. At higher magnifications,  $\text{MgO}$  dendritic crystallites were identified, which are oriented in the direction perpendicular to the substrate surface (**Figure 18c**).

The  $\text{MgO}$  layer has a developed surface with well-defined elongated grains, which demonstrates the growth direction of individual grains. Based on the surface microtopography of the  $\text{MgO}$  layer (**Figure 19a**), it is revealed that there exist grain

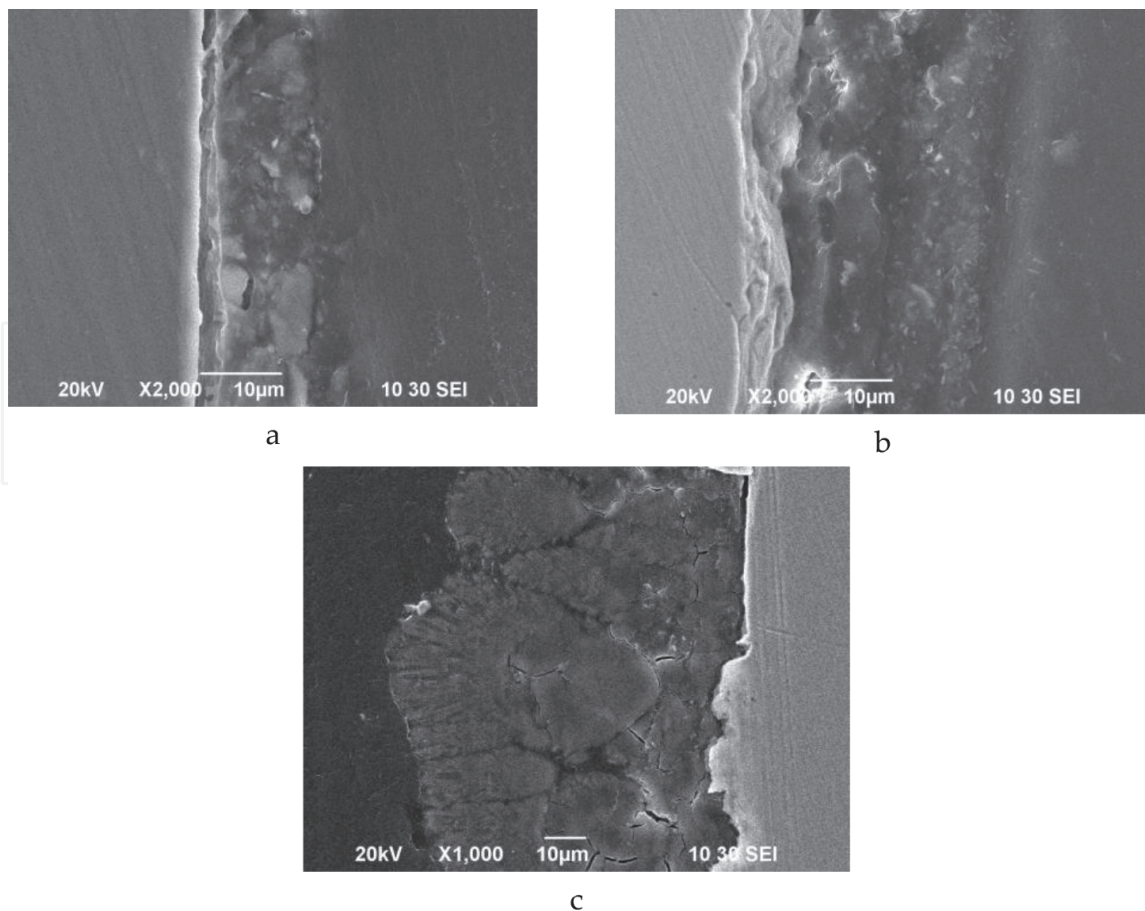


**Figure 18.**  
 SEM microstructure of polished transverse microsections by the depth of oxide layers (a) Al<sub>2</sub>O<sub>3</sub>, (b) TiO<sub>2</sub>, and (c) MgO [2].

clusters along with the individual grains. Each cluster of the size of 200–400 nm is separated by smaller grains (60–150 nm). Similarly to the case of MgO, the outer TiO<sub>2</sub> sublayer has a developed surface with well-defined projections, gaps, and grain boundaries (**Figure 19b**). The TiO<sub>2</sub> surface is characterized by a spheroidal, row-like structure that could have been formed as a result of local instability of the plasma combustion. The disorientation of TiO<sub>2</sub> grains may be due to the high concentration of plasma on the substrate surface and the intensity of heat removal from the substrate. Grain clusters of the size of 50–100 nm in the structure of the TiO<sub>2</sub> sublayer are aggregated into packages up to 500 nm in size. More precise studies of the topology of the outer Al<sub>2</sub>O<sub>3</sub> sublayer made it possible to clearly identify grain boundaries and quantify grain size gradation (**Figure 19c**). The microrelief of the Al<sub>2</sub>O<sub>3</sub> surface has a dimple structure which is oriented perpendicularly to the surface [4].

In order to estimate the increase in the loss current and the breakdown voltage of the dielectric layers, the electrical characteristics were investigated for an alternating current case. To obtain the electrical characteristics of the coating, the upper contact made of foil was pressed against its surface, and an electrode was applied over the foil. As the lower contact, a steel substrate was used. Measurements of capacitance (*C*) and tangent of dielectric loss angle (*tg δ*) at frequencies of 120 Hz, 1 kHz, 10 kHz, and 100 kHz were performed by bridge method using RLC meter in the mode of the parallel equivalent circuit with a measurement error of 0.05%.

The electrical conductivity values for Al<sub>2</sub>O<sub>3</sub>, MgO, and TiO<sub>2</sub> coatings at low frequencies are almost unchanged at room temperature and are approximately  $3 \times 10^{-8} \text{ Ohm}^{-1} \text{ m}^{-1}$ ,  $7 \times 10^{-8} \text{ Ohm}^{-1} \text{ m}^{-1}$ , and  $3 \times 10^{-8} \text{ Ohm}^{-1} \text{ m}^{-1}$ , respectively. In dielectric layers of Al<sub>2</sub>O<sub>3</sub> (at temperatures above 300°C) and MgO



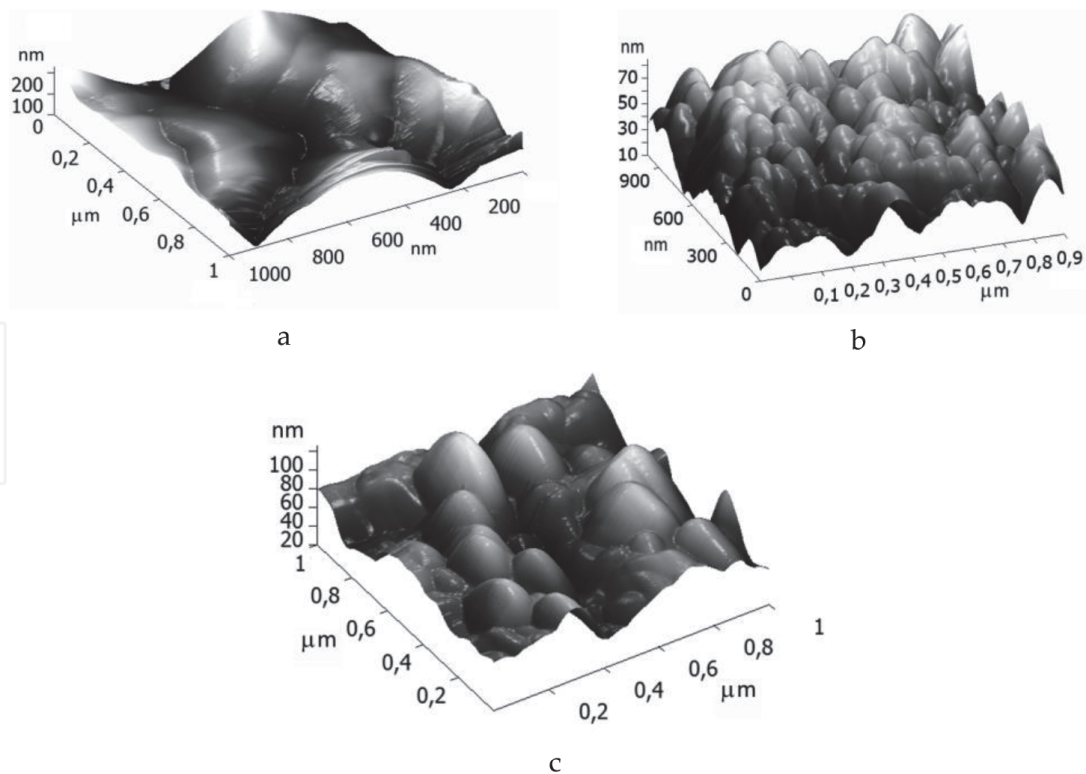


**Figure 19.** AFM surface microtopography of the dielectric layers (a) MgO, (b) TiO<sub>2</sub>, and (c) Al<sub>2</sub>O<sub>3</sub> [2].

(at temperatures above 150°C), a monotonous increase in conductivity begins, caused by the thermal activation of charge carriers from energy levels of 0.63 eV and 0.35 eV, respectively. The electrical conductivity of TiO<sub>2</sub> coatings decreases from  $4 \times 10^{-8} \text{ Ohm}^{-1} \text{ m}^{-1}$  to  $1 \times 10^{-10} \text{ Ohm}^{-1} \text{ m}^{-1}$  with increasing temperature from room temperature to 250°C and increases to  $1 \times 10^{-7} \text{ Ohm}^{-1} \text{ m}^{-1}$  with increasing temperature up to 400°C [2].

As can be seen from the temperature dependences of the electrical conductivity of the dielectric layers for an alternating current case, in all investigated coating systems with increasing frequency, the magnitude of the electrical conductivity increases linearly. The increase in  $\sigma(\omega)$  is due to the delay of slow polarization mechanisms. Moreover, the exponent  $n$  in the equation  $\sigma(\omega) = \omega^n$  for the studied materials differs: for the Al<sub>2</sub>O<sub>3</sub> layers  $n = 0.2$ , whereas for MgO  $n = 0.5$ . For titanium oxide coatings, it increases to 0.9.

Thus, the peculiarities of formation of the structure, adhesive, micromechanical, and electrophysical properties of the Al<sub>2</sub>O<sub>3</sub>, TiO<sub>2</sub>, and MgO dielectric layers obtained by ion-plasma sputtering were established. An optimal mode of formation of Al<sub>2</sub>O<sub>3</sub>, TiO<sub>2</sub>, and MgO dielectric layers was also determined: the gas pressure in the range  $P = (1.5\text{--}4) \times 10^{-2} \text{ mmHg}$ , the arc current in the range  $I = 30\text{--}40 \text{ A}$ , the displacement potential on substrate  $E = -60 \text{ V}$ , and the time  $\tau = 20 \text{ min}$ .

When selecting the material for the substrate and dielectric layer during the design of a film heating element, it is necessary to evaluate the type and order of values of the dielectric losses that occur under operating conditions.

#### 4. Conclusion

The existing methods for producing insulating coatings on the surface of corrosion-resistant steels are analyzed. It is shown that the CVD methods (ion-plasma deposition of metal oxide metal) of deposition on stainless steel substrates

make it possible to obtain high-quality dielectric coatings for film heating elements with high micromechanical and electrophysical properties. The disadvantage of this method is its low productivity, which makes it impossible to use it in mass production. The relevance of using highly efficient and low-cost methods for the synthesis of functional coatings based on glass-ceramic glass sealants is shown. This method is simpler in execution technology and cheaper considering the use of raw materials, which opens up wide prospects for use in mass production. Given the proportionality of the sizes of coatings formed by both methods, the identity of the structure, microtopography of the surface, and the level of electrophysical properties, it can be argued that the first method can be recommended for applying dielectric coatings on the surface of stainless steels which is used for creating film heating elements.

### Author details


Zoia Duriagina<sup>1,2\*</sup>, Taras Kovbasyuk<sup>1</sup>, Volodymyr Kulyk<sup>1</sup>, Andriy Trostianchyn<sup>1</sup> and Tetiana Tepla<sup>1</sup>

<sup>1</sup> Lviv Polytechnic National University, Lviv, Ukraine

<sup>2</sup> John Paul II Catholic University of Lublin, Lublin, Poland

\*Address all correspondence to: [zduriagina@ukr.net](mailto:zduriagina@ukr.net)

### IntechOpen

© 2020 The Author(s). Licensee IntechOpen. This chapter is distributed under the terms of the Creative Commons Attribution License (<http://creativecommons.org/licenses/by/3.0>), which permits unrestricted use, distribution, and reproduction in any medium, provided the original work is properly cited. 

## References

- [1] Duryahina ZA, Borysyuk AK, Bespalov SA, Pidkova VY. Influence of the thermal cyclic treatment on the phase composition of ion-nitrided surface layers of 12KH18N10T steel. *Materials Science*. 2012;**48**:364-368. DOI: 10.1007/s11003-012-9514-x
- [2] Duriagina ZA, Kovbasyuk TM, Bespalov SA. The analysis of competitive methods of improvement of operational properties of functional layers of flat heating elements. *Uspehi Fiziki Metallov*. 2016;**17**:29-51. DOI: 10.15407/ufm.17.01.029
- [3] Duriagina Z, Kovbasyuk T, Bialopiotrowicz T, Bespalov S. Energy state and micromechanical properties of PbO-ZnO-B<sub>2</sub>O<sub>3</sub> glass-ceramic functional coatings on AISI420 stainless steel substrate. *Functional Materials*. 2017;**24**: 250-255. DOI: 10.15407/fm24.02.250
- [4] Duriagina Z, Kovbasyuk T, Zagula-Yavorska M, Bespalov S, Drajewicz M, Dychtoń K, et al. Comparative estimation of the structure and electrical properties of functional layers based on PbO-ZnO-B<sub>2</sub>O<sub>3</sub> glass ceramic sealant. *Powder Metallurgy and Metal Ceramics*. 2016;**9/10**:580-584. DOI: 10.1007/s11106-017-9842-3
- [5] Duryahina ZA, Kovbasyuk TM, Bespalov SA, Pidkova VY. Micromechanical and electrophysical properties of Al<sub>2</sub>O<sub>3</sub> Nanostructured dielectric coatings on plane heating elements. *Materials Science*. 2016;**52**: 50-55. DOI: 10.1007/s11003-016-9925-1
- [6] Park SS, Jung KS, Kim BW, Lee SE, Park HC. Microwave heating induced crystallisation of PbTiO<sub>3</sub> from a PbO-B<sub>2</sub>O<sub>3</sub>-ZnO-TiO<sub>2</sub> glass joined to alumina. *Glass Technology*. 2002;**43**: 70-74
- [7] Cheng Y, Xiao H, Guo W. Effects of GeO<sub>2</sub> on structure and properties of PbO-B<sub>2</sub>O<sub>3</sub>-ZnO glass. *Journal of Inorganic Materials*. 2006;**21**:533-538
- [8] Cheng Y, Xiao H, Guo W. Thermal behavior of GeO<sub>2</sub> doped PbO-B<sub>2</sub>O<sub>3</sub>-ZnO-Bi<sub>2</sub>O<sub>3</sub> glasses. *Materials Science and Engineering: A-Structural Materials Properties Microstructure and Processing*. 2006;**423**:184-188. DOI: 10.1016/j.msea.2005.09.130
- [9] Cheng Y, Xiao H, Guo W. Influence of compositions on sealing temperature and properties of lead borate non-crystallizing sealing glasses. *Materials Science and Engineering: A-Structural Materials Properties Microstructure and Processing*. 2007;**464**:210-215. DOI: 10.1016/j.msea.2007.01.146
- [10] Hasheminia S, Nemati A, Eftekhari Yekta B, Alizadeh P. Preparation and characterisation of diopside-based glass-ceramic foams. *Ceramics International*. 2012;**38**:2005-2010. DOI: 10.1016/j.ceramint.2011.10.035
- [11] Ma R, Xiao B, Ma N, Du P. Low-loss insulating-conductive ceramic composite with giant permittivity and high permeability using glass phase as separating layer. *Ceramics International*. 2016;**42**:4126-4135. DOI: 10.1016/j.ceramint.2015.11.085
- [12] Riley BJ, Vienna JD, Frank SM, Kroll JO, Peterson JA, Canfield NL, et al. Glass binder development for a glass-bonded sodalite ceramic waste form. *Journal of Nuclear Materials*. 2017;**489**: 42-63. DOI: 10.1016/j.jnucmat.2017.03.041
- [13] Andreola F, Barbieri L, Lancellotti I, Leonelli C, Manfredini T. Recycling of industrial wastes in ceramic manufacturing: State of art and glass case studies. *Ceramics International*. 2016;**42**:13333-13338. DOI: 10.1016/j.ceramint.2016.05.205

- [14] Subba Rao A, Ashok J, Suresh B, Naga Raju G, Venkatramaiah N, Ravi Kumar V, et al. Physical characteristics of  $\text{PbO}-\text{ZrO}_2-\text{SiO}_2:\text{TiO}_2$  glass ceramics embedded with  $\text{Pb}_2\text{Ti}_2\text{O}_6$  cubic pyrochlore crystal phase: Part-I electrical properties. *Journal of Alloys and Compounds*. 2017;**712**:672-686. DOI: 10.1016/j.jallcom.2017.04.100
- [15] Subba Rao A, Kityk IV, Ashok J, Ravi Kumar V, Plucinski KJ, Reddy ASS, et al. Physical characteristics of  $\text{PbO}-\text{ZrO}_2-\text{SiO}_2:\text{TiO}_2$  glass ceramics embedded with  $\text{Pb}_2\text{Ti}_2\text{O}_6$  cubic pyrochlore crystal phase: Part-II piezo-optical acoustic and elastic properties. *Journal of Alloys and Compounds*. 2017;**725**:318-325. DOI: 10.1016/j.jallcom.2017.07.158
- [16] Siva Sesha Reddy A, Brik MG, Suresh Kumar J, Graça MPF, Naga Raju G, Ravi Kumar V, et al. Structural and electrical properties of zinc tantalum borate glass ceramic. *Ceramics International*. 2016;**42**:17269-17282. DOI: 10.1016/j.ceramint.2016.08.022
- [17] Marczevska A, Środa M, Nocuń M. Thermal and spectroscopic characterization of gallium-tellurite glasses doped  $\text{BaF}_2$  and  $\text{PbO}$ . *Journal of Non-Crystalline Solids*. 2017;**464**: 104-114. DOI: 10.1016/j.jnoncrysol.2017.03.026
- [18] Jakkula S, Deshpande V. Effect of  $\text{MgO}$  addition on the properties of  $\text{PbO}-\text{TiO}_2-\text{B}_2\text{O}_3$  glass and glass-ceramics. *Ceramics International*. 2013;**39**:S15-S18. DOI: 10.1016/j.ceramint.2012.10.027
- [19] Duan F. The role of  $\text{PbO}$  on crystallization in  $\text{PbO}-\text{SrO}-\text{TiO}_2-\text{SiO}_2$  glass. *Journal of Non-Crystalline Solids*. 2010;**356**:2286-2288. DOI: 10.1016/j.jnoncrysol.2010.07.041
- [20] Sharif A, Gan CL, Chen Z. Customized glass sealant for ceramic substrates for high temperature electronic application. *Microelectronics Reliability*. 2014;**54**:2905-2910. DOI: 10.1016/j.microrel.2014.07.005
- [21] Białopiotrowicz T. Influence of erroneous data on the results of calculations from acid-base surface free energy theories. I. Simulations for a small input data set. *Journal of Adhesion Science and Technology*. 2007;**21**: 1539-1556. DOI: 10.1163/156856107782793230
- [22] Białopiotrowicz T. Influence of erroneous data on the results of calculations from acid-base surface free energy theories. II. Why are negative values of square roots obtained. *Journal of Adhesion Science and Technology*. 2007;**21**:1557-1573. DOI: 10.1163/156856107782793221
- [23] Białopiotrowicz T. Influence of erroneous data on results in acid-base surface free energy theories calculations. III. Solution of a three-equation set in the case of homoscedastic error. *Journal of Adhesion Science and Technology*. 2009;**23**:799-813. DOI: 10.1163/156856108X396327
- [24] Białopiotrowicz T. Influence of erroneous data on results in acid-base surface free energy theories calculations. IV. Solution of an overdetermined set in the case of homoscedastic error. *Journal of Adhesion Science and Technology*. 2009;**23**:815-825. DOI: 10.1163/156856108X396336
- [25] Della Volpe C, Siboni S. Some reflections on acid-base solid surface free energy theories. *Journal of Colloid and Interface Science*. 1997;**95**:121-136. DOI: 10.1006/jcis.1997.5124
- [26] Jańczuk B, Białopiotrowicz T, Zdziennicka A. Some remarks on the components of the liquid surface free energy. *Journal of Colloid and Interface Science*. 1999;**211**:96-103. DOI: 10.1006/jcis.1998.5990



- [27] Gleiter H. Nanocrystalline materials. *Progress in Materials Science*. 1989;**33**: 223-314
- [28] Gleiter H. Nanostructured materials: Basic concepts and microstructure. *Acta Materialia*. 2000;**48**:1-29. DOI: 10.1016/0079-6425(89)90001-7
- [29] Palumbo G, Erb U, Aust K. Triple line disclination effect on the mechanical behavior of materials. *Scripta Metallurgica et Materialia*. 1990; **24**:1347-1350. DOI: 10.1016/0956-716X(90)90091-T
- [30] Sun NX, Lu K. Heat-capacity comparison among the nanocrystalline amorphous and coarse-grained polycrystalline in Se. *Physical Review B*. 1996;**54**:6058-6061. DOI: 10.1103/PhysRevB.54.6058
- [31] Zhao YH, Lu K. Grain size dependence of thermal properties of nanocrystalline Se studied by means of X-ray diffraction. *Physical Review B*. 1997;**56**:14330-14337
- [32] Sharma I, Sharma A, Barman PB. Electrical properties of magnesium oxide thin films. *Optoelectronics and Advanced Materials—Rapid Communications*. 2008;**2**:640-642
- [33] Bondoux C, Prené P, Belleville P, et al. MgO insulating films prepared by sol-gel route for SiC substrate. *Journal of the European Ceramic Society*. 2005; **25**:2795-2798. DOI: 10.1016/j.jeurceramsoc.2005.03.142
- [34] Kim TW, You YS. Microstructural and electrical properties of MgO thin films grown on p-InP (100) substrates at low temperature. *Applied Surface Science*. 2001;**180**:162-167. DOI: 10.1016/S0169-4332(01)00335-X
- [35] Shin D-Y, Kim K-N. Electrical and optical properties of MgO films deposited on soda lime glass by a sol-gel process using magnesium acetate. *Journal of Ceramic Processing Research*. 2009;**10**:536-540
- [36] Afanasov IM, Lazoryak BI, editors. *High Temperature Ceramic Fibers*. Moscow: Tutorial; 2010. p. 51 (in Russian)
- [37] Stevens JE, Sowa MJ, Cecchi JL. Helicon plasma source excited by a flat spiral coil. *Journal of Vacuum Science & Technology A*. 1995;**13**:2476-2482. DOI: 10.1116/1.579491
- [38] Duriagina ZA, Pidkova VY, Olshevska SO. Structure peculiarities and properties of magnesium oxide layers formed by a hybrid ion-plasma discharge system. *Functional Materials*. 2013;**20**:192-197. DOI: 10.15407/fm20.02.192